DTU Library

Smart Sensor Based Obstacle Detection for High-Speed Unmanned Surface Vehicle

Hermann, Dan; Galeazzi, Roberto; Andersen, Jens Christian; Blanke, Mogens

Link back to DTU Orbit

Smart Sensor Based Obstacle Detection for High-Speed Unmanned Surface Vehicle

D. Hermann [*] **R. Galeazzi** [*] **J. C. Andersen** [*] **M. Blanke** [*,**]

[*] *Automation and Control Group, Dept. of Electrical Engineering, Technical University Denmark, Lyngby, Denmark (e-mail: {danh, rg, jca, mb}@elektro.dtu.dk).*
[**] *AMOS CoE, Dept. of Engineering Cybernetics, Norwegian University of Science and Technology, Trondheim, Norway.*

Abstract: This paper describes an obstacle detection system for a high-speed and agile unmanned surface vehicle (USV), running at speeds up to 30 m/s. The aim is a real-time and high performance obstacle detection system using both radar and vision technologies to detect obstacles within a range of 175 m. A computer vision horizon detector enables a highly accurate attitude estimation despite large and sudden vehicle accelerations. This further facilitates the reduction of sea clutter by utilising a attitude based statistical measure. Full scale sea trials show a significant increase in obstacle tracking performance using sensor fusion of radar and computer vision.

1. INTRODUCTION

An unmanned surface vehicle (USV), which should perform autonomous operations, requires local situation awareness by sensing the immediate environment to avoid collision with obstacles on the sea surface. A key requirement to autonomous operation is that information about the surroundings is obtained and processed sufficiently fast to enable safe manoeuvring. The vehicle in focus on this paper is a high-speed personal water craft (PWC) that has been modified for intelligent control aiming at unmanned autonomous operation.

Obstacle detection at sea was treated in literature for larger and less agile vehicles using e.g a 360° rotating radar on a catamaran (Almeida et al., 2009) and a small vessel (Schuster et al., 2014); a laser scanner on a channel barge (Ruiz and Granja, 2008). A solely vision-based solution for a high-speed USV was presented in (Wang et al., 2011). For highly manoeuvrable and fast vehicles a range finder without moving parts and independence of light conditions is desirable, as these vehicles are exposed to forces up to 10g during wave crest impacts at full speed even at moderate sea state.

Within the last decade the development towards assisting driving systems for the automotive industry has made Electronically Scanning Radar (ESR) systems commonly available. The automotive radars are generally characterised by a short detection range up to 200 m and a narrow vertical field of view (FOV). This represents a challenge for the considered type of vehicle because pitch and roll motion may cause potential obstacles to be periodically located in a blind spot. Another challenge is posed by the sea clutter, i.e. reflections that occur when the angle of attack of the radar's beam to the sea surface increases due to waves (Skolnik, 2001). In the automotive industry

sensor fusion of range finders and computer vision has been used to enhance robustness of obstacle detection, as shown in (Coue et al., 2003; Gidel et al., 2009; Monteiro et al., 2006).

This paper proposes a sensor fusion strategy of radar and vision technologies further supplemented with dedicated filtering and statistical methods to obtain robust results for marine operations of highly manoeuvrable and fast planing crafts. First vehicle position and attitude filters are robustified by using the on-board camera as additional aiding sensor. A vision-based horizon detection is exploited to provide additional measurements of roll and pitch angles. Then a methodology is developed to track obstacles temporarily by means of computer vision while they are outside the radar's FOV, and merge information when the obstacle becomes in view of both sensors. Sea clutter reduction is tackled by utilizing an estimate of the probability of false detection based on the attitude of the craft and the radar detection angle relative to the sea surface.

Design of a real-time horizon and obstacle detectors are shown to be essential tools for the algorithms to detect single obstacles that move relative to the body frame of the vessel. Moreover a multiple obstacle tracker (MOT) is designed to fuse radar and computer vision to increase the robustness of the tracker. Sea tests demonstrate the ability of the algorithms to make reliable and robust obstacle detection over a range of operational conditions.

The paper is structured as follows. The design of position and attitude filters using sensor fusion with computer vision horizon detection is addressed in Section 3. The design of a real-time horizon and obstacle detectors are treated in Section 4. The design of the multiple obstacle tracker by means of sensor fusion of radar and camera
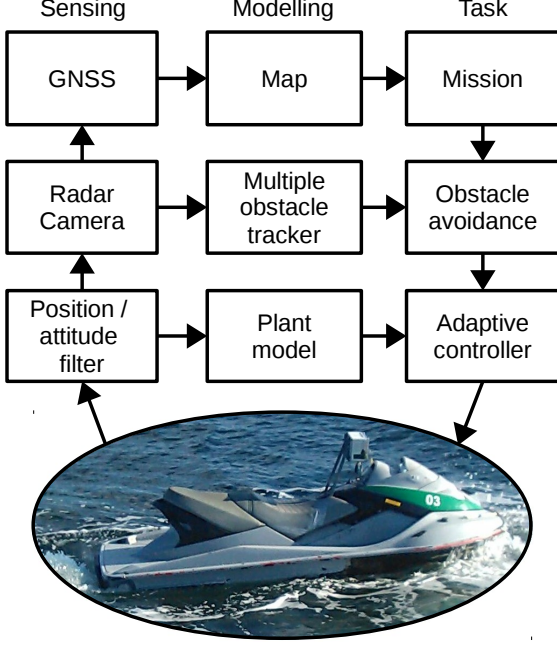
Fig. 1. System architecture - NASREM model.

information is presented in Section 5. Full-scale sea trials results are analysed in Section 6.

2. SYSTEM CONFIGURATION

The USV is a commercial PWC of type Sea Doo GTX 215, modified by the Royal Danish Naval Weapons School for military drills. A 32-bit dual-core (1.6 GHz) Linux based computer is used, facilitating real-time data processing. During sea trials only position and attitude estimation were fully implemented. The computer is located in the bulk with standard navigation sensors: 6-DOF IMU and 3-DOF magnetometer (100 Hz) as well as GNSS $(3 - 4\,\text{Hz})$. On top of the vehicle a Delphi ESR 915 (77 GHz) automotive radar is mounted together with a camera with 640×480 pixels resolution. The vision system has a $52° \times 39°$ FOV and it is sampled at 10 frames per second (FPS). The radar scans in front of the vehicle every 50 ms with a vertical FOV of $5°$ in both long range mode of 175 m $(\pm 15°)$ and middle range mode of 50 m $(\pm 45°)$, Fig. 2.

The overall system architecture is shown in Fig. 1 using the NASREM model (Albus et al., 1989), where the first steps for plant modelling and $\mathcal{L}_1$ adaptive controllers for way-point navigation and station keeping were conducted by Svendsen et al. (2012) and Theisen et al. (2013), respectively.
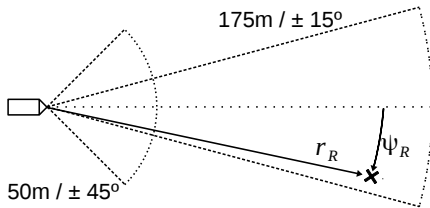
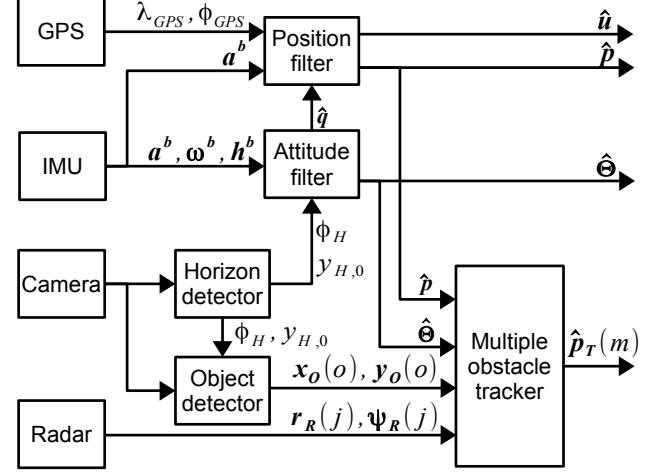

Fig. 2. Radar middle and long range areas.
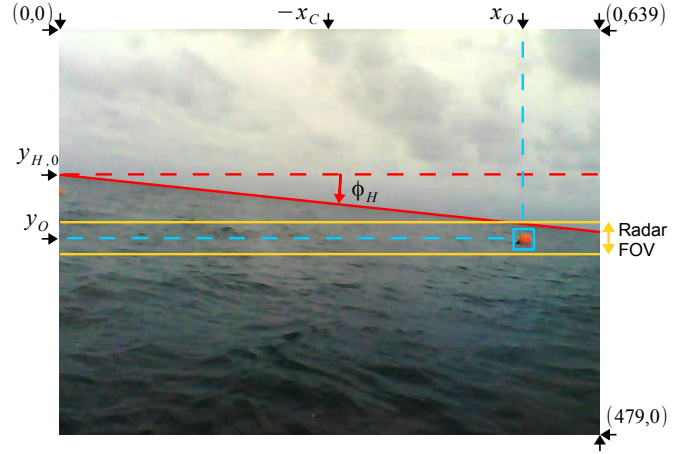

Fig. 3. System block diagram.

Fig. 4. Radar vertical FOV and the camera FOV.

Figure 3 shows the system block diagram for the position and attitude filters, and the multiple obstacle tracker. Figure 4 shows a camera image that displays an indication of the radar vertical FOV (yellow), the position of the detected obstacle (x_O, y_O) (blue) and the estimated horizon line given by $(y_{H,0}, \phi_H)$ (red).

3. POSITION AND ATTITUDE FILTER

As the range finder provides the candidate object position relatively to the drone, accuracy of the drone position $\hat{\boldsymbol{p}} = [\hat{N}, \hat{E}, \hat{D}]^{\mathrm{T}}$ and attitude $\hat{\boldsymbol{\Theta}} = [\hat{\phi}, \hat{\theta}, \hat{\psi}]^{\mathrm{T}}$ estimates is vital to reduce the variance on the obstacle position $\boldsymbol{p}_T$. An accurate attitude estimate will also be beneficial to the statistical measure used for separation of valid obstacles and sea clutter. This exploits the radar detection angle relative to the sea surface (θ_D) that is obtained from the estimated roll $(\hat{\phi})$ and pitch $(\hat{\theta})$ angles and the radar detection angle (ψ_R). Therefore an estimation error less than $2°$ for $\hat{\phi}$ and $\hat{\theta}$ is desired.

Attitude estimators are often implemented as integration filters of the angular rate gyroscope measurements $\boldsymbol{\omega^b}$, where $\hat{\phi}$ and $\hat{\theta}$ are corrected with respect to gravity by linear accelerometer measurements $\boldsymbol{a^b}$, and $\hat{\psi}$ is corrected by either magnetometer $\boldsymbol{h^b}$ or course over ground from

the GNSS (Fossen, 2011). The b superscript refers to the forward-right-down (XYZ) body frame and n to the global north-east-down (NED) navigation frame. The rotation matrix for conversion from body to navigation frame using quaternions is given by

$$R_b^n(\boldsymbol{q}) = \begin{bmatrix} 1 - 2(q_2^2 + q_3^2) & 2(q_1q_2 - q_3q_0) & 2(q_1q_3 + q_2q_0) \\ 2(q_1q_2 + q_3q_0) & 1 - 2(q_1^2 + q_3^2) & 2(q_2q_3 - q_1q_0) \\ 2(q_1q_3 - q_2q_0) & 2(q_2q_3 + q_1q_0) & 1 - 2(q_1^2 + q_2^2) \end{bmatrix} \quad (1)$$

and $R_n^b(\boldsymbol{q}) = (R_b^n(\boldsymbol{q}))^{\mathrm{T}}$.

In Lima and Torres (2012) four state-of-the-art attitude filters recently published were compared by means of simulation. The maximum absolute pitch estimation error for the best performing filter during three different flight scenarios were 0.64°, 2.7°, and 6.7° respectively. In addition the PWC hull is imposed by severe wave crest impacts at high speed causing significant disturbances to the measurements of linear acceleration. Hence an additional roll and pitch reference (ϕ_C and θ_C) obtained from the horizon line in the on-board camera image is essential to achieve the desired accuracy and robustness to disturbances.

The filter implementation is shown in the system block diagram Fig. 3, using two distinct Kalman filters for position and attitude estimation.

3.1 Position Estimation

The model integrates the measured linear acceleration $\boldsymbol{a}^b$ to obtain estimates of the velocity $\hat{\boldsymbol{v}}$ and the position $\hat{\boldsymbol{p}}$ state estimates. Let $\hat{\boldsymbol{x}}_P = [\hat{\boldsymbol{p}}^{\mathrm{T}}, \hat{\boldsymbol{v}}^{\mathrm{T}}]^{\mathrm{T}}$ be the state vector, $\boldsymbol{u}_P = [\boldsymbol{a}^{b,\mathrm{T}}, g]^{\mathrm{T}}$ be the input vector, and $\boldsymbol{y}_P = \boldsymbol{p}^n$ be the measurement vector then the mechanization model is given by

$$\dot{\hat{\boldsymbol{x}}}_P = \begin{bmatrix} \hat{\boldsymbol{v}} \\ R_b^n(\hat{\boldsymbol{q}})\boldsymbol{a}^b - \boldsymbol{g} + \boldsymbol{\eta}_a \end{bmatrix} \quad (2)$$

where $\boldsymbol{g}$ is the gravity vector in the navigation frame, $\hat{\boldsymbol{q}}$ is the estimated quaternion vector, and $\boldsymbol{\eta}_a$ is zero mean white process noises. The estimated observation vector is given by $\hat{\boldsymbol{y}}_P = h_P(\hat{\boldsymbol{x}}_P) = \hat{\boldsymbol{p}}^n$.

3.2 Attitude Estimation

The attitude estimator is designed as an integration filter, where the orientation is obtained from the measured angular velocity $\boldsymbol{\omega}^b$ and represented in quaternions $\boldsymbol{q}$. The filter includes a bias estimate $\boldsymbol{b}_\omega^b$ of the measured angular velocity from the rate gyroscope in order to increase the accuracy (Lima and Torres, 2012).

Let $\hat{\boldsymbol{x}}_A = [\hat{\boldsymbol{q}}^{\mathrm{T}}, \hat{\boldsymbol{b}}_\omega^{b,\mathrm{T}}]^{\mathrm{T}}$ be the state vector, $\boldsymbol{u}_A = \boldsymbol{\omega}^b$ be the input vector then the mechanization model is given by

$$\dot{\hat{\boldsymbol{x}}}_A = \begin{bmatrix} \frac{1}{2} \begin{bmatrix} -\hat{q}_1 & -\hat{q}_2 & -\hat{q}_3 \\ \hat{q}_0 & -\hat{q}_3 & \hat{q}_2 \\ \hat{q}_3 & \hat{q}_0 & -\hat{q}_1 \\ -\hat{q}_2 & \hat{q}_1 & \hat{q}_0 \end{bmatrix} (\boldsymbol{\omega}^b - \hat{\boldsymbol{b}}_\omega^b) \\ \boldsymbol{\eta}_b \end{bmatrix} \quad (3)$$

where $\boldsymbol{\eta}_b$ is zero mean white processes noise driving the bias estimate $\hat{\boldsymbol{b}}_\omega^b$.

The measurement vector is $\boldsymbol{y}_A = [\boldsymbol{a}^{b,\mathrm{T}}, \boldsymbol{h}^{b,\mathrm{T}}, \phi_C, \theta_C]^{\mathrm{T}}$, where the magnetic inclination angle $\theta_H = 70°$ at the test location, and ϕ_C and θ_C are the roll and pitch observations
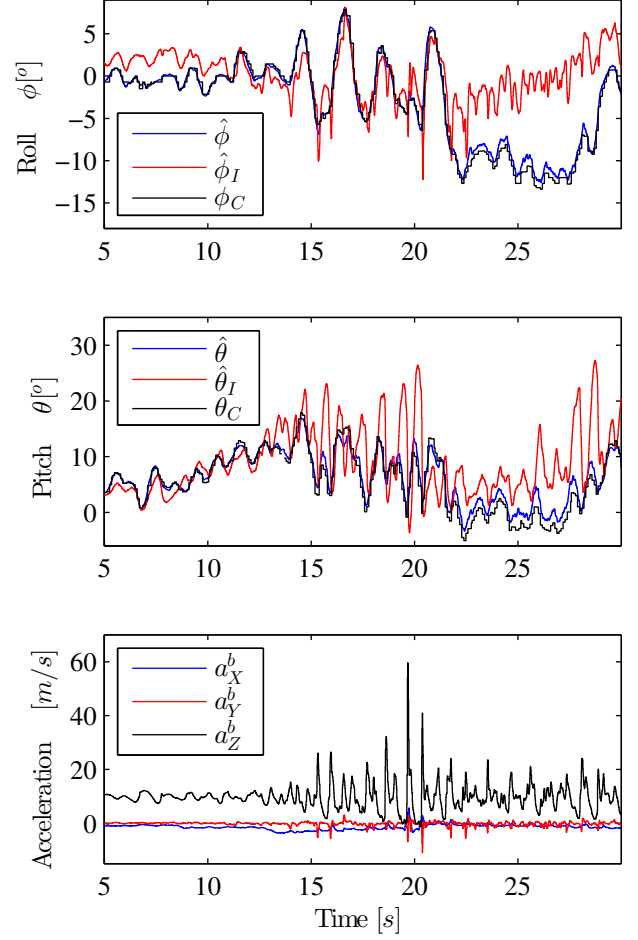

Fig. 5. Estimated attitude during sea trial in slight sea conditions.

obtained from the detected horizon line, see Fig. 4. The two Euler angle observations are given by $\phi_C = -\phi_H$ and $\theta_C = \arctan((y_{H,0} - x_C \sin(\theta_H) - y_{\Delta,C})\alpha_C)$, where x_C is the horizontal position of the centre pixel, α_C is the camera focal length and $y_{\Delta,C}$ is the camera pitch offset in pixels. The estimated output vector is given by

$$\hat{\boldsymbol{y}}_A = h_A(\hat{\boldsymbol{x}}_A) = \begin{bmatrix} R_n^b(\hat{\boldsymbol{q}})[0, 0, g]^{\mathrm{T}} \\ R_n^b(\hat{\boldsymbol{q}})[\cos(\theta_H), 0, \sin(\theta_H)]^{\mathrm{T}} \\ \arctan\left(R_{b,32}^n(\hat{\boldsymbol{q}})/R_{b,33}^n(\hat{\boldsymbol{q}})\right) \\ -\arcsin(R_{b,31}^n(\hat{\boldsymbol{q}})) \end{bmatrix} \quad (4)$$

3.3 Kalman Filter Update

The discrete time implementation of the position estimator runs at $f_S = 100\,\mathrm{Hz}$ and it is corrected by the Kalman Filter when a GNSS update is available at $f_{S,G} \simeq 3.5\,\mathrm{Hz}$.

The extended Kalman filter for attitude estimation runs at $100\,\mathrm{Hz}$ and the correction by ϕ_C and θ_C, which are provided by the vision system, takes place at $f_{S,C} = 10\,\mathrm{Hz}$.

3.4 Attitude Filter Test

The attitude estimates from a test sequence of the USV operating in slight sea is shown in Fig. 5. The roll and pitch estimates ($\hat{\phi}, \hat{\theta}$) are significantly improved by means of

the horizon detection from the on-board camera (ϕ_C, θ_C), compared to the estimates $(\hat{\phi}_I, \hat{\theta}_I)$ obtained only using IMU and magnetometer. The roll and pitch estimates are robust to hull impact disturbances at high speed $(30\,\text{m/s})$ occurring after 15 s. Note the severe impacts to the roll and pitch estimates $\hat{\phi}_I$ and $\hat{\theta}_I$ from the linear acceleration measurements $\boldsymbol{a}^b$.

4. COMPUTER VISION

4.1 Horizon Line Detector

First a bow-tie shaped mask is applied to the blue channel of the input image (Fig. 6(a)) located around the horizon line detected in the previous image in order to select the region of interest (ROI). The mask is given by the maximum anticipated roll (λ_ϕ) and pitch (λ_θ) rates between consecutive images, based on sea trial data. If no previous horizon line estimate is available, the horizon line search is performed using the full input image. A Canny edge detector is then applied to find edges in the image, see white and red edge detections in Fig. 6(b). The Canny edge detector is selected as it provides a good detection of soft edges, though it is computationally heavier than simpler methods, as e.g. threshold of images filtered with Prewitt or Sobel masks (Canny, 1986; Gonzalez et al., 2009). This feature increases robustness of the horizon detector with land in the horizon. A line detection algorithm is implemented, that first removes all pixels without a neighbour pixel to left, right or in a corner position, and then retain coherent lines of minimum n_c pixels in the Canny image (red edge detection in Fig. 6(b)) and yield horizon line candidates given by

$$y = y_{H,0} + x\sin(\phi_H). \tag{5}$$

The filter retains horizontal lines and thus reduce the number of lines occurring from of waves and drops on the lens. All horizon line candidates fulfilling the aforementioned criteria are evaluated using the cost function

$$\begin{aligned}\Gamma(l,f) =& |\phi_C(l,f) - \phi_C(f-1)|\eta_\phi + |\theta_C(l,f) - \theta_C(f-1)|\eta_\theta \\ &+ \varepsilon_L(l)\eta_L - \varepsilon_E(l)\eta_E\end{aligned} \tag{6}$$

with the line index l and iterative frame index f. The first two terms describe the change in roll and pitch angles between consecutive images, $\varepsilon_L(l)$ characterises the line straightness using the length of the individual (red) edge detections relative to the distance between the end points, and $\varepsilon_E(l)$ the number of pixels (line fill) from the Canny image contained in the line given in (5) for the full image width. The four weights in the cost function for roll change (η_ϕ), pitch change (η_θ), line straightness (η_L) and line fill (η_E) are chosen based on sea trial data. The horizon line candidate l with the lowest cost is chosen as the horizon line for the frame f.

4.2 Obstacle Detector

The texture patterns for the sea surface are in a relatively steady-state most of the time, thus obstacles appears salient in the image, Fig. 7(a). The approached method applies an adaptive threshold (Gonzalez et al., 2009) with a 45×45 pixel mask to the saturation image in Fig. 7(b), in order to detect obstacles. Interconnected regions in the threshold image below the horizon line of size
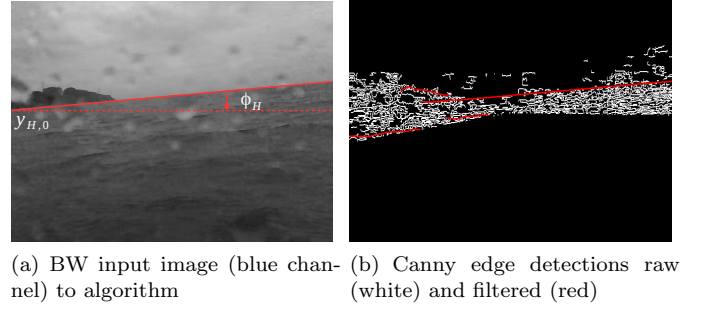

(a) BW input image (blue channel) to algorithm

(b) Canny edge detections raw (white) and filtered (red)

Fig. 6. Images from the horizon detection algorithm.

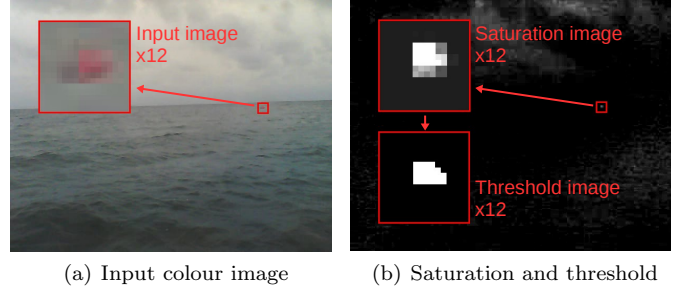(a) Input colour image

(b) Saturation and threshold

Fig. 7. Images from the obstacle detection algorithm.

s_O larger than the threshold v_s are accepted as obstacle candidates, Fig. 7(b). Each obstacle is reference by its centre pixel position x_O and y_O. The captured image in 6(a) is acquired in overcast conditions. An algorithm robust to the changing light condition at sea is required for a final implementation relaying on the camera for obstacle detection.

5. MULTIPLE OBSTACLE TRACKER

A reliable methodology for obstacle identification and tracking is essential in order to automatically detect objects of interest and suppress clutter. The multiple obstacle tracker consists of three processing blocks, as shown in Fig. 8. The *Filtering and Prediction* block updates the known track positions $\hat{\boldsymbol{p}}_T(m)$ using measurement candidates from the radar given by range $r_R(j)$ and horizontal angle $\psi_R(j)$ for $j = \{1, 2 \ldots n_J\}$ as well as camera image position $x_O(o)$ and $y_O(o)$ for $o = \{1, 2 \ldots n_O\}$ assigned by the *Gating and Association* block, where n_J and n_O is the number of obstacles candidates from radar and computer vision respectively. Following the persistence score γ is updated and evaluated in the *Track Maintenance* block for each track.
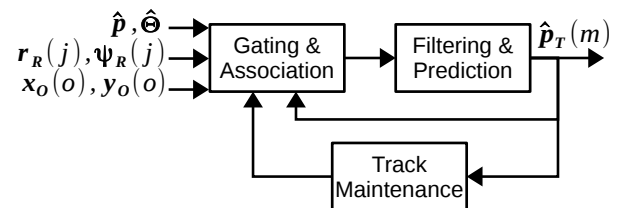

Fig. 8. Block diagram of the multiple obstacle tracker.

5.1 Filtering and Prediction

The tracked objects are modelled using a constant velocity model, with the state vector $\hat{\boldsymbol{x}}_T(m) = [\hat{\boldsymbol{p}}_T(m)^{\mathrm{T}}, \hat{\boldsymbol{v}}_T(m)^{\mathrm{T}}]^{\mathrm{T}}$, where the position and velocity in the navigation frame are given by $\hat{\boldsymbol{p}}_T(m) = [\hat{p}_{T,N}(m), \hat{p}_{T,E}(m)]^{\mathrm{T}}$ and $\hat{\boldsymbol{v}}_T(m) = [\hat{v}_{T,N}(m), \hat{v}_{T,E}(m)]^{\mathrm{T}}$. The state-space model is given in (7) and the estimated observation vector is given in (8), where $\boldsymbol{\eta}_u$, $\boldsymbol{\eta}_r$ and η_o are the zero mean white noise processes.

$$\dot{\hat{\boldsymbol{x}}}_{\boldsymbol{T}}(m) = \begin{bmatrix} \hat{\boldsymbol{v}}_T(m) \\ \boldsymbol{\eta}_u \end{bmatrix} \tag{7}$$

$$\begin{bmatrix} \hat{\boldsymbol{y}}_R(m) \\ \hat{y}_C(m) \end{bmatrix} = \begin{bmatrix} \hat{\boldsymbol{p}}_T(m) + \boldsymbol{\eta}_r \\ \arctan\left(\dfrac{\hat{\boldsymbol{p}}_{T,N}(m) - \hat{\boldsymbol{p}}_N}{\hat{\boldsymbol{p}}_{T,E}(m) - \hat{\boldsymbol{p}}_E}\right) + \eta_o \end{bmatrix} \tag{8}$$

The observation vector $\boldsymbol{y}_T(j,o) = [\boldsymbol{y}_R(j)^{\mathrm{T}}, y_C(o)]^{\mathrm{T}}$ consists of the north-east position components $\boldsymbol{y}_R(j) = [p_{R,N}(j), p_{R,E}(j)]^{\mathrm{T}}$ from the observed radar position in the navigation frame

$$\boldsymbol{p}_R(j) = \hat{\boldsymbol{p}} + R_b^n(\hat{\boldsymbol{q}}) R_r^b (0, \theta_\Delta, \psi_R(j)) (r_R(j) \; 0 \; 0)^T,$$

where R_r^b is the rotation matrix from the radar-frame to the body-frame and θ_Δ is the vertical radar pitch alignment angle. The yaw detection angle of the vision system is given by

$$y_C(o) = \psi_O(o) = \hat{\psi} + (x_O(o) - x_C)\alpha_c \cos(\hat{\theta}).$$

For a one DOF constant velocity model, the resulting process noise covariance matrix Q_T can be expressed as

$$Q_T = \sigma_{p0} \begin{bmatrix} T_{S,R}^3/3 & T_{S,R}^2/2 \\ T_{S,R}^2/2 & T_{S,R} \end{bmatrix}$$

where $T_{S,R}$ is the radar sampling period (Blackman and Popoli, 1999). The covariance matrix of the observation noise is given in Eqs. (9)-(11).

$$R_R(j) = \begin{bmatrix} \sigma_N^2(j) & 0 \\ 0 & \sigma_E^2(j) \end{bmatrix}, \qquad R_C = \sigma_{\psi_C}^2 \tag{9}$$

$$\sigma_N^2(j) \simeq [\sigma_{\psi_R} r_R(j) \sin(\hat{\psi} + \psi_R(j)]^2 + [\sigma_r \cos(\hat{\psi} + \psi_R(j))]^2 \tag{10}$$

$$\sigma_E^2(j) \simeq [\sigma_{\psi_R} r_R(j) \cos(\hat{\psi} + \psi_R(j))]^2 + [\sigma_r \sin(\hat{\psi} + \psi_R(j))]^2 \tag{11}$$

The track position is predicted and corrected using an extended Kalman filter, where the discrete gain matrices for radar K_R and vision system K_C are computed individually. The obstacle state estimate $\hat{\boldsymbol{x}}_T$ is updated using either K_R, K_C or $K_T = [K_R, K_C]$ along with the relevant measurement update ($\boldsymbol{y}_R$, y_C or $\boldsymbol{y}_T$). For a one DOF constant velocity model the initial prediction error covariance matrix is set according to (12), (Blackman and Popoli, 1999).

$$P_{T,0} = \begin{bmatrix} \sigma_{p0}^2 & 0 \\ 0 & \sigma_{v0}^2 \end{bmatrix} = \begin{bmatrix} 1 & 0 \\ 0 & 25 \end{bmatrix} \tag{12}$$

5.2 Gating and Association

The task of the obstacle association procedure is to assign track update candidates from the radar and the vision system. The first step is a gating procedure to determine which observations are valid candidates to update an existing track.

A relative distance $d_R(j,m,k)$ between the predicted track position and the candidate position for iteration index k is computed for the radar candidate position in (13) and evaluated using the closeness criteria $c_R(j,m,k)$ in (14).

$$d_R(j,m,k) = \frac{(\hat{\boldsymbol{p}}_{T,N}(m,k) - \boldsymbol{p}_{T,N}(j,k))^2}{\sigma_N^2(j,k)} \tag{13}$$
$$+ \frac{(\hat{\boldsymbol{p}}_{T,E}(m,k) - \boldsymbol{p}_{T,E}(j,k))^2}{\sigma_E^2(j,k)}$$

$$c_R(j,m,k) = 3\sqrt{\sigma_N^2(j,k) + \sigma_E^2(j,k) + \sigma_{pN}^2(m,k) + \sigma_{pE}^2(m,k)} \tag{14}$$

All distances fulfilling the gate $d_R(j,m,k) < c_R(j,m,k)$ are accepted for track association. The closeness criteria utilise the measurement noise ($\sigma_N^2(j,k)$, $\sigma_E^2(j,k)$) and the state prediction error covariance matrix $\hat{P}_R(m)$ from the EKF position estimation. Here $c_R(j,m,k)$ corresponds to three times the standard deviation of the prediction error, hence 99.7% of all true detections will be accepted as as track updates.

Obstacles detected by the vision system are tracked in the image using the distance $d_C(o,m,k)$ (15), where the first term describes the yaw angle difference and second term the change in distance from the horizon line from the previous image, (16). For the initial image ($k = 0$) the second term is given by the distance to the relative centre position of the radar beam in the image y_R using (17). The closeness criteria in (18) is chosen based on sea trial data.

$$d_C(o,m,k) = (\hat{\psi}_O(m,k) - \psi_O(o,k))^2 \tag{15}$$
$$+ ((d_{C,H}(o,m,k) - d_{C,H}(o,m,k-1))\alpha_C)^2$$

$$d_{C,H}(o,m,k) = y_O(o,k)\cos(\phi_H(k)) - \tag{16}$$
$$(y_{H,0}(k) + x_O(o,k)\sin(\phi_H(k)))\cos(\phi_H(k))$$

$$d_{C,H}(o,m,0) = (\hat{\psi}_O(m,0) - \psi_O(o,0))^2 \tag{17}$$
$$+ ((y_O(o,0) - y_R)\alpha_C)^2$$

$$c_C = (10° \cdot 2\pi/360)^2 \tag{18}$$

For each iteration the $n_T = |\mathcal{M}|$ tracks are matched with n_J and n_O update candidates from the radar and vision system respectively, where $\mathcal{M}$ is the set of active tracks. All are matched one-to-one, that is one candidate can only be assigned to one track and vice versa.

The matching process is conducted in three steps, where tracks are assigned using the Global Nearest Neighbour (GNN) method. That is matching the radar and vision candidates to the tracks one-by-one using $d_R(j,m,k)$ and $d_C(o,m,k)$ respectively as a cost function for all unmatched candidates

(1) Candidates are matched to confirmed tracks
(2) Unmatched candidates are matched to the non-confirmed tracks
(3) All unmatched radar candidates initialises a new track

Note that a track cannot be initialised by a detection from the vision system alone.

5.3 Track Maintenance

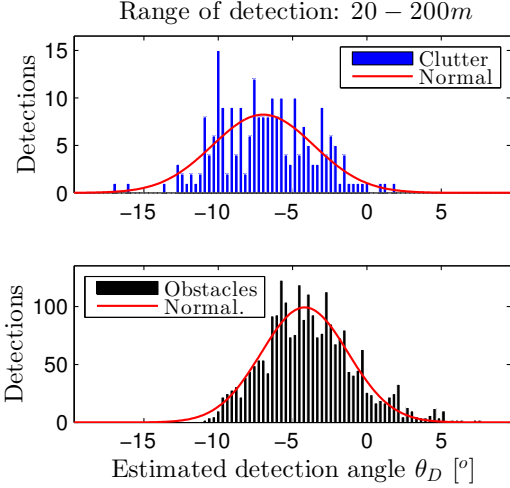In principle when an observation from the radar cannot be associated to a track, a new track should be initialised

Fig. 9. Detection segmentation histogram from estimated height $\boldsymbol{\theta}(D)$.

and considered a valid track. As both the radar and camera do provide a considerable number of false detections, it is desirable to introduce a validation of the initiated tracks. Various methods exits for track evaluation, where the simplest is referred to as the *M/N ad-hoc* rule, which requires an observation to be present in at least $M > N$ consecutive frames, to be confirmed as a track.

The method applied here is instead the Sequential Probability Ratio Test (SPRT) (Blackman and Popoli, 1999), which uses a recursively updated persistence score including signal related and kinematic information in the persistence measure $\gamma(m, k)$, Eqs. (19)-(21).

$$\gamma(m,k) = \gamma(m,k-1) + \underbrace{\gamma_{\Delta S}(m,k)}_{\text{signal part}} + \underbrace{\gamma_{\Delta K}(m,k)}_{\text{kinematic part}}$$

(19)

$$\gamma_{\Delta S}(m,k) = \ln\left(\frac{P_D(x)}{P_{FA}(x)}\right)$$

(20)

$$\gamma_{\Delta K}(m,k) = \ln\left(\frac{V_C}{\sqrt{|S(m,k)|}}\right) - \frac{M\ln(2\pi) + d_R(j,m,k)}{2}$$

(21)

The signal related term is a log-likelihood measure given by the probability of detection (P_D) and probability of false alarm (P_{FA}), which either can be chosen as static parameters or to be dependent variables. By utilising training data from sea trials at open sea all radar detections are segmented into the classes of detection (H_O) and clutter (H_C) using the manual defined object segmentation circles, see Fig. 9 and Fig. 11. For the detection D, the probabilities of obstacle and clutter are defined as $P_D = P(D|H_O)$ and $P_{FA} = P(D|H_C)$ respectively. A Gaussian distribution yield an adequate description the probability density of obstacles ($p_O(\theta_D)$) and clutter ($p_C(\theta_D)$) detection using the detection angle

$$\theta_D = -\arcsin\left([R^n_{b,31}, R^n_{b,32}, R^n_{b,33}] \times \right.$$

(22)

$$\left. [\cos(\psi_R)\cos(\theta_\Delta), \sin(\psi_R)\cos(\theta_\Delta), -\sin(\theta_\Delta)]^{\mathrm{T}}\right).$$

Their equivalent cumulative distribution functions in (23) and (24) yield the input for (20).

$$P_D(\theta_D) = P_O(\theta_D) \tag{23}$$
$$P_{FA}(\theta_D) = 1 - P_C(\theta_D) \tag{24}$$

The first kinematic term in (21) is given by the radar measurement volume V_C and the track residual determinant

$$S(m,k) = H_R \cdot P_T(m,k|k-1) \cdot H_R^{\mathrm{T}} + R_R(m,k),$$

where H_R is the linearised output matrix from (8). The second kinematic the measurement dimension $M = 2$ and the relative distance $d_R(j,m,k)$ in (13).

A graphical interpretation of the track evaluation from the persistence score is given in Fig. 10. Tracks are initiated with $\gamma = 0$ and evaluated until reaching either the confirmation threshold T_C or the deletion threshold T_D, where a track is respectively confirmed or deleted in the MOT. The persistence score γ cannot exceed T_C. The two thresholds are obtained from the design parameters for false-track-confirmation probability P_{FTC} and the true-track-deletion probability P_{TTD}, which are user defined parameters

$$T_C = \ln\left(\frac{1 - P_{TTD}}{P_{FTC}}\right), \quad T_D = \ln\left(\frac{P_{TTD}}{1 - P_{FTC}}\right) \quad (25)$$
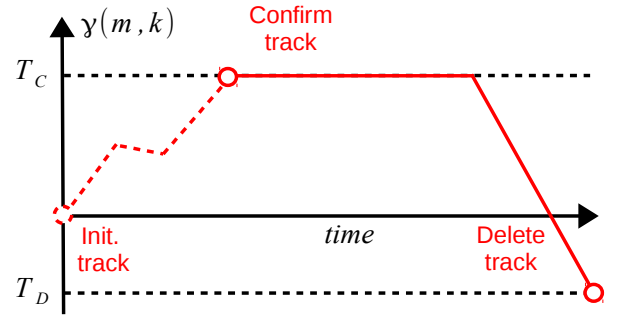

Fig. 10. Persistence score track evaluation procedure

6. RESULTS

Full scale sea trials were conducted in order to verify tracking persistence and performance as well as clutter rejection. During each test sequence four predefined obstacles (buoys) were placed in a distance of approx. 100 m from the coast line and a rubber inflatable boat (RIB) at multiple (static) positions further at sea, see MOT output in Fig. 11. The USV was launched from a pier and remotely controlled by a human operator during the sea trials. The vehicle path is marked alongside with confirmed track position from obstacles and clutter, depending whether inside or outside the segmentation circles respectively. The general procedure was to approach the obstacles at a constant heading angle from a distance exceeding the radar range.

6.1 Clutter rejection

The output map for the MOT using static values of P_{FA} and P_D is shown in Fig. 11. The majority of false detections from sea clutter are already removed from the map, as only confirmed track positions are indicated in the figure. Figure 12 demonstrates that the number
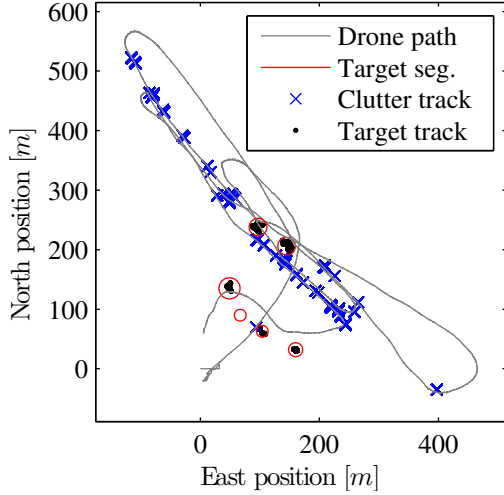
Fig. 11. Map of confirmed obstacles: tracks initiated and updated using radar only.
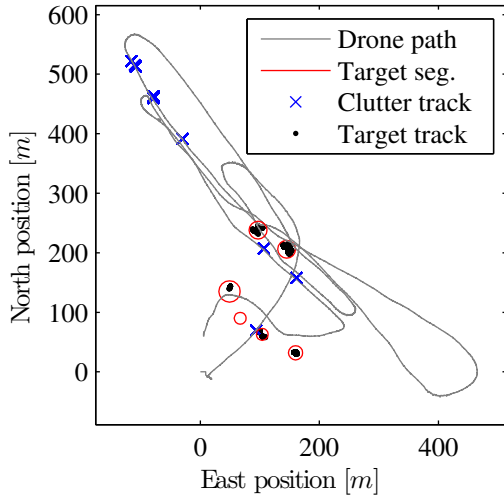

Fig. 12. Map of confirmed obstacles: tacks initiated and updated using radar with clutter statistics.

of confirmed track positions from clutter are reduced while the obstacles in the segmentation circles are still detected in a safe distance, sufficient to perform an evasive manoeuvre.

6.2 Tracking persistence

The drone proceeded the RIB at approx. 20 m/s from a distance above 200 m, see Fig. 13 and Fig. 14. Radar detections not assigned to a confirmed track are marked with blue crosses and the confirmed track with a red line. Four isolated detections occur in a distance from 165 m to 120 m. When only utilising the radar a consistent detection is not obtained before a distance of approx. 100 m, where the first track is confirmed, Fig. 13. A sharp turn causes the MOT to lose track of the RIB at 80 m, until resuming continuous tracking at 60 m. By utilising also the vision-based obstacle detection the RIB is continuously tracked from the first detection at 165 m to the track exceed the radar horizontal FOV in a distance of approx. 20 m, Fig. 14. The use of the vision-based
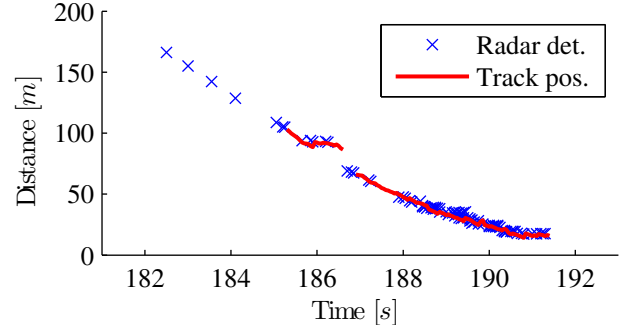

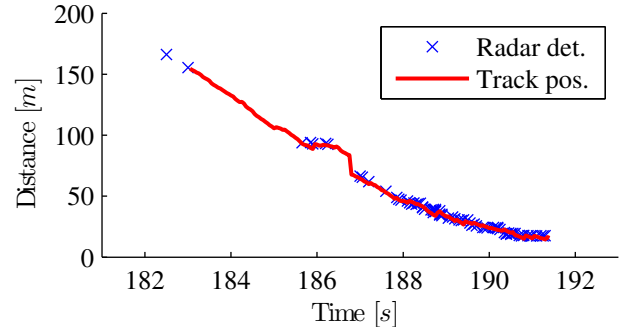Fig. 13. Range of detection of the RIB for tracker initiated and updated using radar only.

Fig. 14. Range of detection of the RIB for tracker initiated from radar and updated using both radar and camera.

obstacle detection yields a significant improvement of the continuous tracking performance.

7. CONCLUSIONS

This paper described an obstacle detection system for a high-speed unmanned surface vehicle with particular focus on track persistence and reduction of sea clutter. A Kalman based position and attitude filters were designed and implemented. The accuracy and precision of the attitude filter was shown to be significantly improved using the horizon estimate from the vision system. A multiple obstacle tracker was further implemented, utilising sensor fusion of radar and vision system. Tracks were successfully maintained by the vision system, also when not appearing in the radar vertical field-of-view due to pitch and roll oscillations, increasing the track persistence and the actual range of detection. A significant clutter reduction at open sea was demonstrated utilising a statistical measure of clutter and obstacle detection obtained from training data.

Future work will focus on connecting previous work on hydrodynamic models and $\mathcal{L}_1$ adaptive controllers for way-point navigation and station keeping with an obstacle avoidance module, see Fig. 1. Use of hydrodynamic models is expected to improve prediction of position and attitude significantly during acceleration and turns, hence the obstacle position estimates during an avoidance manoeuvre. Preliminary work on the design and implementation for path re-planning and a dedicated guidance law using existing $\mathcal{L}_1$ adaptive controllers has been conducted for the obstacle avoidance module.

REFERENCES

Albus, J.S., McCain, H.G., and Lumia, R. (1989). Nasa/nbs standard reference model for telerobot control system architecture (nasrem). Technical report.

Almeida, C., Franco, T., Ferreira, H., Martins, A., Santos, R., Almeida, J., Carvalho, J., and Silva, E. (2009). Radar based collision detection developments on USV ROAZ II. In *Proc. IEEE Conf. OCEANS'09*.

Blackman, S. and Popoli, R. (1999). *Design and Analysis of Modern Tracking Systems*. Artech House.

Canny, J. (1986). A computational approach to edge detection. *IEEE Transactions on Pattern Analysis and Machine Intelligence*, PAMI-8(6), 679–698.

Coue, C., Fraichard, T., Bessiere, P., and Mazer, E. (2003). Using bayesian programming for multi-sensor multi-target tracking in automotive applications. In *Proc. IEEE Int. Conf. on Robotics and Automation, ICRA '03*, volume 2, 2104–2109.

Fossen, T.I. (2011). *Marine Craft Hydrodynamics and Motion Control*. Wiley.

Gidel, S., Blanc, C., Chateau, T., Checchin, P., and Trassoudaine, L. (2009). Non-parametric laser and video data fusion: application to pedestrian detection in urban environment. In *12th Int. Conf. on Information Fusion, FUSION '09.*, 626–632.

Gonzalez, R.C., Woods, R.E., and Eddins, S.L. (2009). *Digital image processing using MATLAB*, volume 2. Gatesmark Publishing Tennessee.

Lima, R. and Torres, L.A.B. (2012). Performance evaluation of attitude estimation algorithms in the design of an AHRS for fixed wing UAVs. In *Robotics Symposium and Latin American Robotics Symposium (SBR-LARS), 2012 Brazilian*, 255–260.

Monteiro, G., Premebida, C., Peixoto, P., and Nunes, U. (2006). Tracking and classification of dynamic obstacles using laser range finder and vision. In *Proc. IEEE/RSJ Int. Conf. on Intelligent Robots and Systems (IROS)*.

Ruiz, A. and Granja, F. (2008). A short-range ship navigation system based on ladar imaging and target tracking for improved safety and efficiency. *IEEE Transac. Intelligent Transportation Systems*, 10(1), 186–197.

Schuster, M., Blaich, M., and Reuter, J. (2014). Collision avoidance for vessels using a low-cost radar sensor. In *Proc. 19th IFAC World Congress*, 9673 – 9678.

Skolnik, M.I. (2001). *Introduction to radar systems*. McGraw-hill New York.

Svendsen, C., Holck, N.O., Galeazzi, R., and Blanke, M. (2012). $\mathcal{L}_1$ adaptive maneuvering control of unmanned high-speed water craft. In *Proc. MCMC2012*.

Theisen, L.R.S., Blanke, M., and Galeazzi, R. (2013). Unmanned water craft identification and adaptive control in low-speed and reversing regions. In *Proc. CAMS2013*.

Wang, H., Wei, Z., Wang, S., Ow, C., Ho, K., Feng, B., and Lubing, Z. (2011). Real-time obstacle detection for unmanned surface vehicle. In *Proc. Defense Science Research Conference and Expo, DSR'2011*.